



# Femtosecond laser micro-structuring of aluminium under helium

W. Perrie<sup>a,\*</sup>, M. Gill<sup>a</sup>, G. Robinson<sup>b</sup>, P. Fox<sup>a</sup>, W. O'Neill<sup>c</sup>

<sup>a</sup>Department of Engineering, University of Liverpool, Brownlow Hill, Liverpool L69 3GH, UK

<sup>b</sup>Center for Manufacturing Engineering, Tennessee Technological University, 115 West Tenth Street, Cookeville, TN 38505, USA

<sup>c</sup>Department of Engineering, Institute For Manufacturing, University of Cambridge, Mill Lane, Cambridge CB2 11RX, UK

Received 30 September 2003; accepted 18 December 2003

Available online 25 March 2004

## Abstract

The interaction of 180 fs, 775 nm laser pulses with aluminium under a flowing stream of helium at ambient pressure have been used to study the material re-deposition, ablation rate and residual surface roughness. Threshold fluence  $F_{th} \sim 0.4 \text{ J cm}^{-2}$  and the volume ablation rate was measured to be  $30 < V < 450 \mu\text{m}^3$  per pulse in the fluence range  $1.4 < F < 21 \text{ J cm}^{-2}$ . The presence of helium avoids gas breakdown above the substrate and leads to improved surface micro-structure by minimising surface oxidation and debris re-deposition. At 1 kHz rep. rate, with fluence  $F > 7 \text{ J cm}^{-2}$  and  $>85 \text{ W cm}^{-2}$  average power density, residual thermal effects result in melt and debris formation producing poor surface micro-structure. On the contrary, surface micro-machining at low fluence  $F \sim 1.4 \text{ J cm}^{-2}$  with low power density,  $\sim 3 \text{ W cm}^{-2}$  produces much superior surface micro-structuring with minimum melt and measured surface roughness  $R_a \sim 1.1 \pm 0.1 \mu\text{m}$  at a depth  $D \sim 50 \mu\text{m}$ . By varying the combination of fluence/scan speed during ultra-fast ablation of aluminium at 1 kHz rep. rate, results suggest that maintaining average scanned power density to  $<5 \text{ W cm}^{-2}$  combined with single pulse fluence  $<4 \text{ J cm}^{-2}$  produces near optimum micro-structuring. The debris under these conditions contains pure aluminium nanoparticles carried with the helium stream.

© 2004 Elsevier B.V. All rights reserved.

PACS: 79.20.D; 42.62.C

Keywords: Femtosecond laser ablation; Micro-machining; Aluminium; Re-deposition

## 1. Introduction

Energetic ( $\mu\text{J}$ – $\text{mJ}$ ) optical pulses with femtosecond pulselengths and hence ultra-high focussed intensities in the range  $10^{12}$  to  $10^{16} \text{ W cm}^{-2}$  have proved capable of ablating a wide range of materials including metals, semi-conductors, ceramics, fibre composites, polymers, biological tissue and dielectrics [1–7]. In this

intensity regime, multi-photon absorption becomes an important absorption mechanism in wide bandgap materials such as fused silica and the potential for unique applications in photonics and bio-medicine have been identified [8]. In the range  $10^{13}$  to  $10^{14} \text{ W cm}^{-2}$ , ionisation of practically any material, metal or dielectric takes place within the temporal pulselength, which is much shorter than electron-ion and heat conduction times (a few ps). Energetic electrons, with energy above the work function can escape from the surface and ions are then accelerated in the electrostatic field caused by charge separation [9].

\* Corresponding author. Tel.: +44-151-794-4918;

fax: +44-151-794-4675.

E-mail address: [wpfemto1@liv.ac.uk](mailto:wpfemto1@liv.ac.uk) (W. Perrie).

A thin highly ionised layer of material expands from the surface well after the optical pulse has been absorbed. This picture is partly confirmed also by vacuum femtosecond ablation studies which demonstrate the dominance of singly charged states of elemental ions and the absence of molecular ions and fragments [10].

Surface melting can virtually be eliminated along with plasma shielding (which takes place in typical nanosecond laser ablation) leading to more efficient energy deposition while simultaneously minimising collateral damage. Consequently, ablation thresholds are also significantly reduced. For example, in the case of aluminium, threshold fluence at 12 ns pulse length and YAG wavelengths of 1.06, 0.523 and 0.355  $\mu\text{m}$  is approximately 60, 24 and 12  $\text{J cm}^{-2}$ , respectively [11] compared to  $F_{\text{th}} \sim 0.4 \text{ J cm}^{-2}$  found here. In stainless steel, at 780 nm, the ablation threshold was observed to reduce from  $\sim 4$  to  $\sim 0.5 \text{ J cm}^{-2}$  at pulse length 3.3 ns and 200 fs, respectively [1] with nanosecond processing showing significant molten material from vapour and liquid phases while femtosecond processing virtually eliminated liquid phase.

Zhu et al. [12] studied micro-hole drilling of thin aluminium foils (1.5–50  $\mu\text{m}$  thick) and a range of other metals in air by 60 fs, 50 ps and 10 ns laser pulses from a Ti-sapphire laser. A significant amount of melting was present in both the ps and ns regimes whereas the femtosecond material removal process was dominated by a solid–vapour transition, hence minimising droplets from the molten phase. Lapczynya et al. [13] demonstrated ultra-high rep. rate ablation of aluminium foils (12.5–200  $\mu\text{m}$  thickness) with 2  $\mu\text{s}$  bursts of 1.2 ps pulses ( $\lambda = 1.05 \mu\text{m}$ ) with 7.5 ns pulse-to-pulse separation for drilling high aspect ratio holes (7:1). This interesting mode of laser fluence delivery appears to combine quasi-CW heating to support rapid etch rates with the advantage of ultra-short laser material interactions for clean ejection of material.

Detailed single and multiple pulse laser ablation studies of aluminium in air at  $\lambda = 800 \text{ nm}$  with pulse lengths of 125 fs [14] and 33 fs [15] clearly demonstrate that aluminium presents a considerable challenge to micro-structuring even with ultra-fast optical pulses.

Industrial laser processing of metals such as stainless steel and aluminium is generally performed in the presence of a fast flowing inert gas such as nitrogen, argon or helium which helps to prevent surface

oxidation while simultaneously removing melt, particulates and vapours [16]. Recently, Sun and Longtin [17] demonstrated the significant advantage of femtosecond drilling of copper in a flowing helium environment when compared to air, nitrogen or neon. Hole features and repeatability were superior and the incidence of debris much reduced. They attribute these advantages to minimising plasma formation above the substrate which results in beam de-focussing and distortion and self-phase modulation which broadens the pulse spectrum.

This work involves a study of kHz femtosecond ablation and micro-structuring of aluminium under helium. Residual surface features, ablation rate, and residual surface roughness are determined by optical microscopy, interferometric microscopy (WYKO NT3300 profilometer) and SEM.

## 2. Experimental

A turnkey femtosecond laser, a Clarke-MXR 2010 system, based on chirped pulse amplification [18] is used here for ultra-fast studies. A mode locked, diode pumped Erbium doped ring fibre laser at 1550 nm whose output is frequency doubled to 775 nm in periodically poled lithium niobate is used to seed a Ti-sapphire regenerative amplifier. The laser system delivers  $\sim 1 \text{ mJ}$  per pulse at 1 kHz rep. rate and  $\lambda = 775 \text{ nm}$ , 180 fs pulse length and observed bandwidth  $\delta\lambda \sim 5.5 \text{ nm}$  (Pulsoscope autocorrelator with spectrometer, APE Angewandte Physik und Electronic GmbH). Beam intensity spatial profile is near Gaussian with a measured 3D Gaussian fit parameter  $\sim 0.87$  (Spyricon LBA300 with Pulnix TM745E CCD camera). The beam is slightly elliptical, 4.8 mm  $\times$  5.2 mm and shows some residual astigmatism, probably due to cavity design incorporating a Brewster cut Ti-sapphire crystal in the regenerative amplifier. The enclosure temperature is stabilised at 20  $^{\circ}\text{C}$  using a small dedicated chiller (VWR Scientific Products) which also keeps the Ti-sapphire crystal temperature stable. Output pulse stability is typically  $\pm 1\%$  ( $1\sigma$ ) while pre-pulse and post-pulse amplitudes were minimised and measured to be  $< 0.2$  and 1.7%, respectively (Coherent power meter/Molelectron pyroelectric detector).

Fig. 1 shows the experimental set-up. The output from the Clarke-CPA 2010 laser system passes

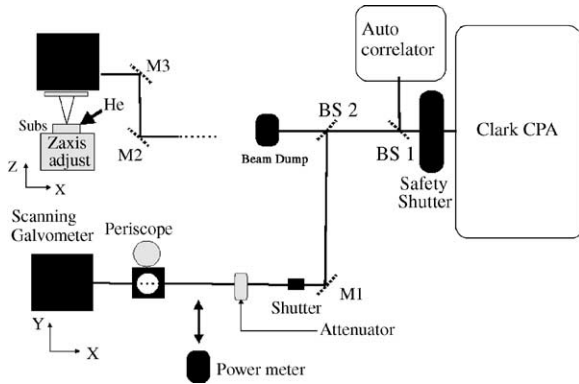


Fig. 1. Schematic diagram of the experimental apparatus.

through a laser safety shutter (Coherent ESA-95), a pick-off beam splitter (BS1) for auto-correlation, then reflected from a 50/50 beam splitter (BS2) and mirror M1 before passing through an attenuator ( $\lambda/2$  plate and Glan laser polariser). The beam is then reflected from a periscope (mirrors M2/M3), and enters a Scanning Galvo head (GSI Lumonics) and focussed with a 100 mm focal length  $f$ - $\theta$  lens AR coated for 780 nm. Transmission through the scan head (mirrors and lenses) was measured to be  $>97\%$ . However, above 150  $\mu\text{J}$  pulse energy, the transmission dropped slightly, probably due to multi-photon absorption in the lens elements. Hence, pulse energies  $\leq 150 \mu\text{J}$  were normally used to avoid non-linear effects which might damage the  $f$ - $\theta$  lens system. A simple gas nozzle which created an inert gas environment was directed to the substrate area of interest with flow rate of around  $30 \text{ cm}^3 \text{ s}^{-1}$ . The effectiveness of this approach was demonstrated by the observed difference in debris, and surface oxidation relative to air, nitrogen and argon.

Scan patterns were software generated (SCAPS GmbH) which allowed materials micro-machining to be investigated. The flat field region is approximately 70 mm square. The spot size  $2\omega_0$  ( $1/e^2$ ) diameter at the focal plane was estimated to be  $\sim 30 \mu\text{m}$  from observed single pulse ablation craters (plot of  $D^2$  versus  $\ln(E_p)$ ) while a diffraction limited spot size ( $1/e^2$ ) diameter is  $\sim 20 \mu\text{m}$  for a Gaussian beam.

The substrates were 2 inch square, 1 mm thick cold rolled aluminium (Goodfellows Metals Ltd.) with  $>99.99\%$  purity and the helium was industrial grade with 99.998% purity. The aluminium surface relief

shows peaks and troughs aligned in one direction due probably to the rolling process. Consequently, the surface roughness is less when measured parallel to these surface features than when measured perpendicular to them.  $R_a$  (parallel) was measured to be  $0.30 \pm 0.05 \mu\text{m}$  while  $R_a$  (perpendicular) was measured to be  $0.50 \pm 0.07 \mu\text{m}$  ( $\pm 1\sigma$ ).

The substrate was positioned on the horizontal surface of a 1 in. mirror mount which was fixed to a vertical high resolution Lab jack (ThorlabsLJ750) with 10  $\mu\text{m}$  resolution. This combination allowed for tilt and vertical adjustment of the substrate surface relative to the beam waist and to the normal to the optic axis of the  $f$ - $\theta$  lens. The depth of focus is given by  $\text{DOF} = (8\lambda/\pi)(f/D)^2$ , where  $\lambda = 0.775 \mu\text{m}$  is the wavelength,  $f = 100 \text{ mm}$  is the lens focal length and  $D = 5.0 \text{ mm}$  is the raw beam diameter before the  $f$ - $\theta$  lens. Using these values, the  $\text{DOF} \sim 800$  or  $\pm 400 \mu\text{m}$ , and would indicate that substrate positioning is not that critical. In practice, the substrate surface needed to be brought to within  $\pm 50 \mu\text{m}$  of the focal plane because of the residual astigmatism in the beam which otherwise resulted in an elliptical profile above and below the focal plane.

### 3. Results and discussion

Preliminary investigations on the femtosecond processing of aluminium under air, nitrogen and argon were disappointing and generated rough and darkened surfaces with excessive amounts of debris in and around the ablated regions.

The use of helium however significantly improved the situation, reducing debris considerably and, under optimum processing conditions, surface reflectivity remained high when the ablated region was viewed with an optical microscope. Even so, an important observation during the femtosecond micro-machining of aluminium under helium was that the combination of fluence/scan speed of the focussed spot on the substrate surface was an important parameter and, when varied, led to a remarkable change in observed surface micro-structure, roughness and debris formation.

The energy deposited per unit area per second (average power density,  $\text{W cm}^{-2}$ ) at the material surface as the focussed spot scans is given approximately by,

$\langle I \rangle \sim (vE_p/\phi s)$ , [ $s \neq 0$ ], where  $v = 10^3$  Hz,  $E_p$  is the pulse energy (J),  $\phi$  is the spot diameter ( $3 \times 10^{-3}$  cm) and  $s$  is the scan speed ( $\text{cm s}^{-1}$ ). This parameter gives a useful indication of the likely residual thermal effects which can lead to detrimental micro-machining and varies here in the range  $3\text{--}500 \text{ W cm}^{-2}$ .

The effect of varying  $\langle I \rangle$  is demonstrated clearly in a series of SEM images, Fig. 2(a)–(i) where we have

processed aluminium with fluence  $7 \leq F \leq 21 \text{ J cm}^{-2}$  and scan speed  $1 \leq s \leq 10 \text{ mm s}^{-1}$  ( $\langle I \rangle \sim 17\text{--}500 \text{ W cm}^{-2}$ ). A square micro-machining pattern was used with a  $10 \mu\text{m}$  raster providing for significant beam overlap during micro-machining. Fig. 2(a) shows the result of ablation at  $\sim 500 \text{ W cm}^{-2}$  ( $21 \text{ J cm}^{-2}/1 \text{ mm s}^{-1}$ ) where although there is significant material removal, most of the debris has returned to the surface

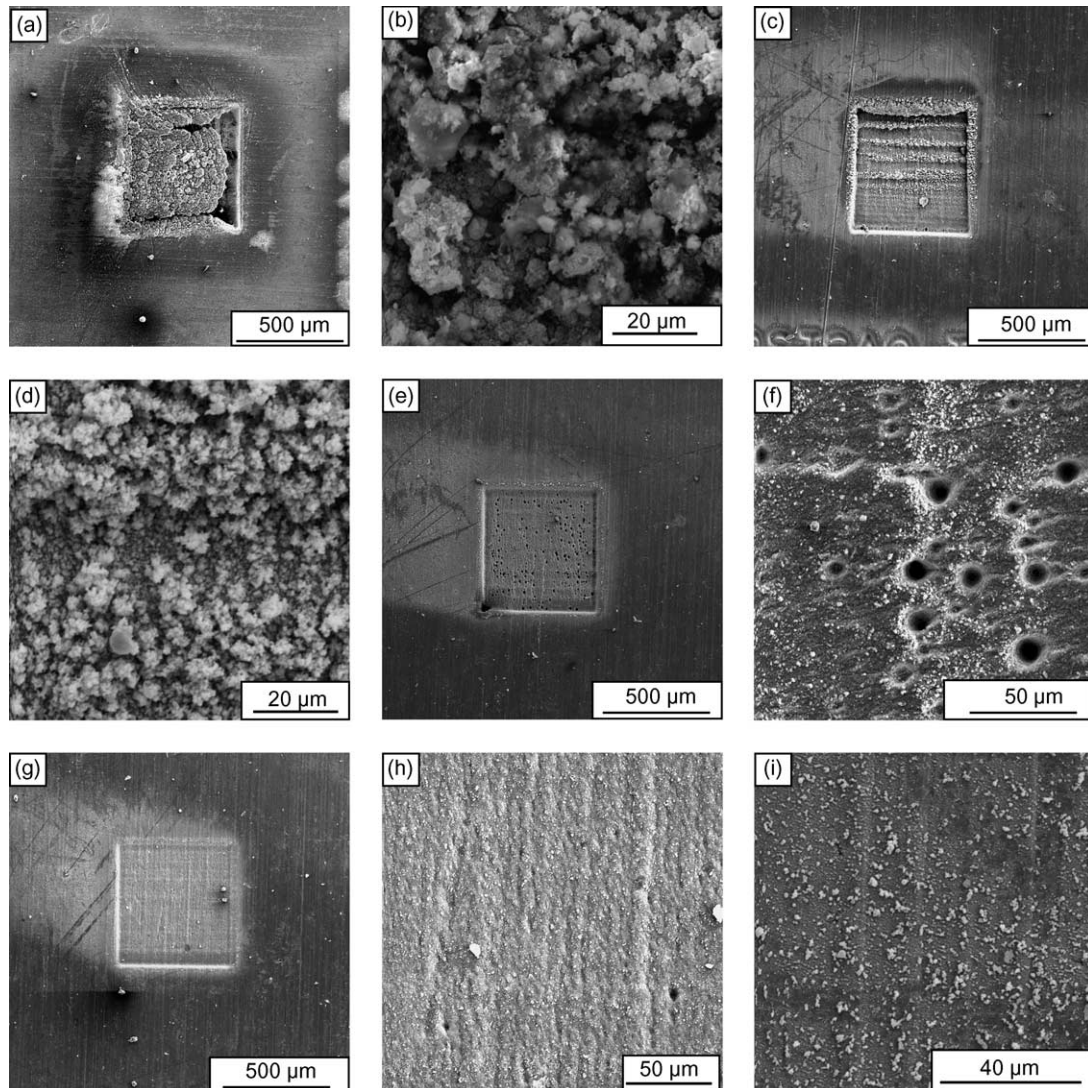


Fig. 2. Femtosecond micro-machining of aluminium under helium at 1 kHz rep. rate and a range of average scanned power densities. (a) and (b)  $500 \text{ W cm}^{-2}$  ( $21 \text{ J cm}^{-2}/1 \text{ mm s}^{-1}$ ). (c) and (d)  $167 \text{ W cm}^{-2}$  ( $7 \text{ J cm}^{-2}/1 \text{ mm s}^{-1}$ ). (e) and (f)  $33 \text{ W cm}^{-2}$  ( $7 \text{ J cm}^{-2}/5 \text{ mm s}^{-1}/5$  overscans). (g) and (h)  $17 \text{ W cm}^{-2}$  ( $7 \text{ J cm}^{-2}/10 \text{ mm s}^{-1}/5$  overscans). (i) Observed debris generated at  $\langle I \rangle \sim 17 \text{ W cm}^{-2}$  carried away with the helium stream.

within the square. Micro-machining aluminium at this high average power density is characterised by surface melting and re-solidification with particulate diameters up to  $20\ \mu\text{m}$  in size, Fig. 2(b). The substantial residual thermal component under these conditions is very detrimental, demonstrating that fs micro-machining of aluminium can give very disappointing results at high average power density.

The beneficial effect of reducing average power density by a factor of 3 to  $\sim 167\ \text{W cm}^{-2}$  ( $7\ \text{J cm}^{-2}/1\ \text{mm s}^{-1}$ ) is shown in Fig. 2(c) and (d). Much more material has left the ablation site, however, there is still significant material re-deposition within the square with debris aligned along the scan direction and melted material still overhanging the machined edges. Fig. 2(d) shows that the particulate re-deposited is finer than in Fig. 2(b) with dimensions up to  $\sim 5\ \mu\text{m}$ . In both cases, the re-deposited material may have subsequently oxidised, indicated by some charging during SEM imaging.

The dramatic effect of reducing average power density by a further factor of 5 to  $\sim 33\ \text{W cm}^{-2}$  ( $7\ \text{J cm}^{-2}/5\ \text{mm s}^{-1}$ ) is shown in Fig. 2(e) and (f). There is very little debris within the square but 5 over-scans to a machined depth of  $\sim 35\ \mu\text{m}$  resulted in the development of small pits. These are up to  $\sim 15\ \mu\text{m}$  wide and  $\sim 12\ \mu\text{m}$  deep, Fig. 2(f). This interesting phenomenon has been observed previously in the UV and NIR fs ablation of semi-conductors such as silicon [19] the onset of which leads to a chaotic deterioration of the surface micro-structure as subsequent ablation couples light strongly into these pits. A brief investigation showed that in aluminium, these pits were produced with linear polarisation when the electric

vector was either parallel or perpendicular to the scan direction. However, the incidence was reduced significantly with circularly polarised light or when the initial surface roughness was polished to  $<0.1\ \mu\text{m rms}$ . There is also a tendency for pit location to be correlated with the initial surface corrugations. This behaviour may have some origin in the initial coupling of the incident radiation with excited surface electromagnetic waves [20,21].

The effect of reducing average power to  $\sim 17\ \text{W cm}^{-2}$  ( $7\ \text{J cm}^{-2}/10\ \text{mm s}^{-1}$ ) is shown in Fig. 2(g) demonstrating efficient femtosecond ablation of aluminium with little material re-deposition within the square, Fig. 2(h). Fine, light coloured debris has been carried away with the helium stream and re-deposited on the adjacent surface. The characteristic surface relief (surface roughness) associated with the pristine surface (cold rolled) is still evident here at a depth of  $\sim 15\ \mu\text{m}$  so that residual surface roughness is still close to  $0.5\ \mu\text{m}$ . This can only happen when melting has been virtually eliminated and the ablation depth per pulse ( $\sim 0.14\ \mu\text{m}$ ), is significantly less than the initial surface roughness  $\sim 0.5\ \mu\text{m}$ . There is evidence also of the onset of pit formation at this depth ( $\sim 15\ \mu\text{m}$ ). Fig. 2(i) shows some of the micron size surface debris carried away with the helium under these conditions.

Single shot ablation of a polished aluminium sample ( $R_a < 0.1\ \mu\text{m}$ ) confirms that to avoid surface melting, low pulse fluence is desirable, Fig. 3(a)–(c). Fig. 3(a), a single shot at fluence  $F \sim 1.4\ \text{J cm}^{-2}$  shows negligible melt and fine surface scratches can still be observed at the centre of the ablated region. At fluence  $F \sim 7\ \text{J cm}^{-2}$ , Fig. 3(b), there is already

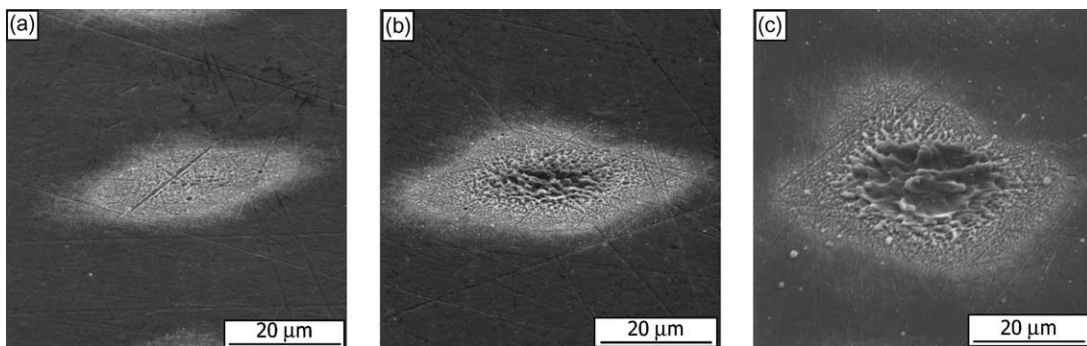


Fig. 3. Single shot femtosecond ablation of polished aluminium. (a)  $1.4\ \text{J cm}^{-2}$ ; (b)  $7\ \text{J cm}^{-2}$ ; (c)  $14.1\ \text{J cm}^{-2}$ .

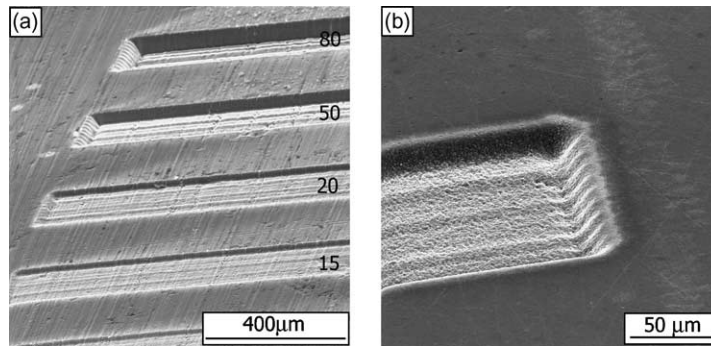


Fig. 4. Femtosecond micro-machining of aluminium under helium at 1 kHz rep. rate and  $\sim 3.3 \text{ W cm}^{-2}$  average power ( $1.4 \text{ J cm}^{-2}/10 \text{ mm s}^{-1}$ ). (a)  $10 \mu\text{m}$  raster with 10/15/20/50/80 overscans. (b)  $240 \mu\text{m}$  wide,  $25 \mu\text{m}$  deep channel on polished aluminium sample micro-machined at  $3.3 \text{ W cm}^{-2}$  average power.

slight surface melting and roughening while at fluence  $F \sim 14 \text{ J cm}^{-2}$ , Fig. 3(c), significant surface melting is very clear with a recast ring around the crater.

These observations all pointed to optimisation of femtosecond materials processing of aluminium under helium by reducing single pulse fluence while keeping average scanned power density low (i.e. keeping scan speed high at around  $10 \text{ mm s}^{-1}$ ). Fig. 4(a) shows a sequence of channels micro-machined at fluence  $1.4 \text{ J cm}^{-2}$  and low average power density ( $3.3 \text{ W cm}^{-2}$ ). The effect of overscanning the pattern up to 80 times can be easily appreciated. Most of the fine debris generated has been carried away with the helium. Fig. 4(b) shows part of a  $240 \mu\text{m}$  wide,  $25 \mu\text{m}$  deep channel machined in this case on a polished aluminium sample ( $R_a < 0.1 \mu\text{m}$ ) and ultrasonically cleaned afterwards in acetone for a few minutes. Note that the surface relief developing here is similar to that with unpolished aluminium with undulations developing parallel to the scan direction and surface reflectivity remained high. Continued overscanning (80 times) resulted in a  $\sim 50 \mu\text{m}$  deep channel with little debris and with surface roughness at the base of the channel measured to be  $R_a = 1.15 \pm 0.1 \mu\text{m}$ , Fig. 5(a), which shows a typical WYKO 2D cross-section. The channels have well defined edges, free of burrs and melt. The wall angles however were high,  $\sim 35^\circ$ , probably related to the near Gaussian laser intensity distribution. The base shows undulations  $\sim 60 \mu\text{m}$  apart ( $\sim 3 \mu\text{m}$  peak–peak) which are due probably to material re-deposition during ablation at ambient pressure under flowing helium. Material re-deposition at ambient pressure affects subsequent ablation and

hence limits final surface roughness. This characteristic surface relief at the track base was observed also when varying raster pitch down to  $2 \mu\text{m}$ .

Fig. 5(b) shows a WYKO 3D colour-coded image of part of a micro-channel machined in aluminium at low average power  $\sim 6.3 \text{ W cm}^{-2}$ , but high fluence and scan speed ( $21 \text{ J cm}^{-2}/80 \text{ mm s}^{-1}/10$  overscans). The surface has developed a periodic structure along the scan direction with pitch  $\sim 80 \mu\text{m}$  corresponding to the pulse-to-pulse separation. While average power thermal effects are low, there is a clear price to pay in surface finish at high fluence. Ablation depth per pulse is high,  $\sim 0.6 \mu\text{m}$  and melt expulsion generates large quantities of debris as one continues micro-machining. Fig. 5(c) shows a 2D  $x$  and  $y$  cross-section of this channel showing that even at this shallow depth of around  $7 \mu\text{m}$ , the peak-to-peak variation is already  $\sim 4 \mu\text{m}$  and grows to  $\sim 7 \mu\text{m}$  at a depth of  $\sim 40 \mu\text{m}$ . An approximately  $60 \mu\text{m}$  period across the channel is apparent, again most likely due to material re-deposition at ambient pressure. The WYKO interferometric microscope can therefore generate information on surface relief, residual surface roughness and from the cross-sectional areas which it computes, ablation rate per pulse.

Fig. 6 shows the measured ablation rate ( $\mu\text{m}^3$  per pulse) of aluminium under helium over the fluence range  $0\text{--}21 \text{ J cm}^{-2}$  with scan speed  $s = 10 \text{ mm s}^{-1}$  ( $\langle I \rangle = 0\text{--}50 \text{ W cm}^{-2}$ ). Threshold fluence is near  $F_{\text{th}} \sim 0.4 \text{ J cm}^{-2}$ . Depths and residual surface roughness were measured with the WYKO profilometer and error bars show  $\pm 1\sigma$  deduced from scatter in measured cross-sections. The corresponding average ablation depth per pulse is  $\sim 47 \text{ nm}$  at  $1.4 \text{ J cm}^{-2}$  while the skin

depth in aluminium  $\delta \sim 14$  nm at  $\lambda \sim 0.775$   $\mu\text{m}$ , estimated from the complex part of the refractive index,  $k = 8.6$  [22]. ( $\delta = 2/\alpha$ , where  $\alpha$ , the absorption coefficient is given by  $\alpha = 4\pi k/\lambda$ ). The ablation depth at fluence  $F \sim 3F_{\text{th}}$  is therefore  $\sim 3$  times the skin depth. As the thermal diffusivity of aluminium is  $D \sim 0.6$   $\text{cm}^2 \text{s}^{-1}$ , the HAZ  $\sim \sqrt{2D\tau} \sim 15$  nm, where  $\tau \sim 2$  ps is the electron–phonon coupling time [23]. These numbers indicate that there probably is a thin melt region a few tens of nm thick created during near threshold femtosecond ablation of aluminium. At high fluence  $F \sim 21$   $\text{J cm}^{-2}$ , the ablation depth per pulse rises to around  $\sim 0.61$   $\mu\text{m}$ .

Fig. 7 shows how channel depth grows with fluence over the range  $1.4\text{--}7$   $\text{J cm}^{-2}$  for 20 overscans at  $10$   $\text{mm s}^{-1}$  scan speed ( $\langle I \rangle \sim 3\text{--}17$   $\text{W cm}^{-2}$ ). The depth machined per overscan ( $10$   $\mu\text{m}$  raster) hence ranges from  $\sim 0.6$  to  $\sim 3$   $\mu\text{m}$  over this fluence range.

Fig. 8 shows the corresponding channel residual surface roughness with fluence at  $10$   $\text{mm s}^{-1}$  scan speed ( $0\text{--}17$   $\text{W cm}^{-2}$ ) for 20 overscans showing how this parameter grows significantly with fluence to around  $1.8 \pm 0.4$   $\mu\text{m}$  from initial value of  $R_a \sim 0.5$   $\mu\text{m}$ .

These results indicated that there is an advantage in keeping fluence as low as practicable, consistent with reasonable processing rates thus minimising

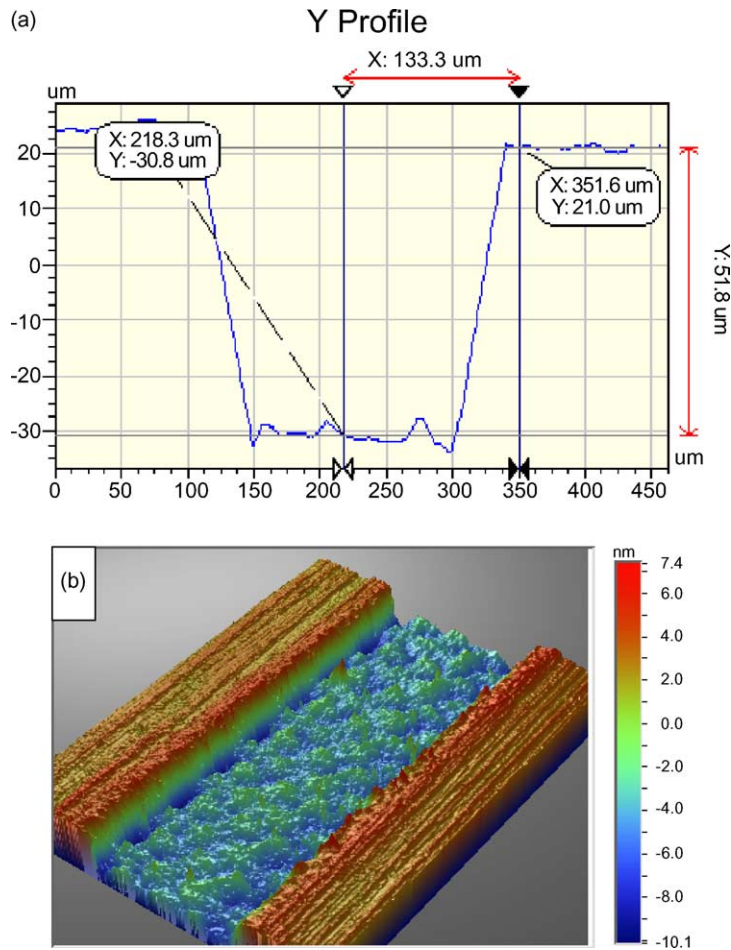


Fig. 5. WYKO images of femtosecond micro-machining of aluminium. (a) cross-section of  $240$   $\mu\text{m}$  wide,  $50$   $\mu\text{m}$  deep channel machined at  $\sim 3.3$   $\text{W cm}^{-2}$  ( $1.4$   $\text{J cm}^{-2}/10$   $\text{mm s}^{-1}$ ) (b) 3D surface relief of  $\sim 7$   $\mu\text{m}$  deep channel micro-machined at  $\sim 6.3$   $\text{W cm}^{-2}$  average power but high fluence ( $21$   $\text{J cm}^{-2}/80$   $\text{mm s}^{-1}/10$  overscans). (c) Typical  $x, y$  surface profile of  $\sim 7$   $\mu\text{m}$  deep channel machined at  $6.3$   $\text{W cm}^{-2}$  and high pulse fluence showing periodic structure.

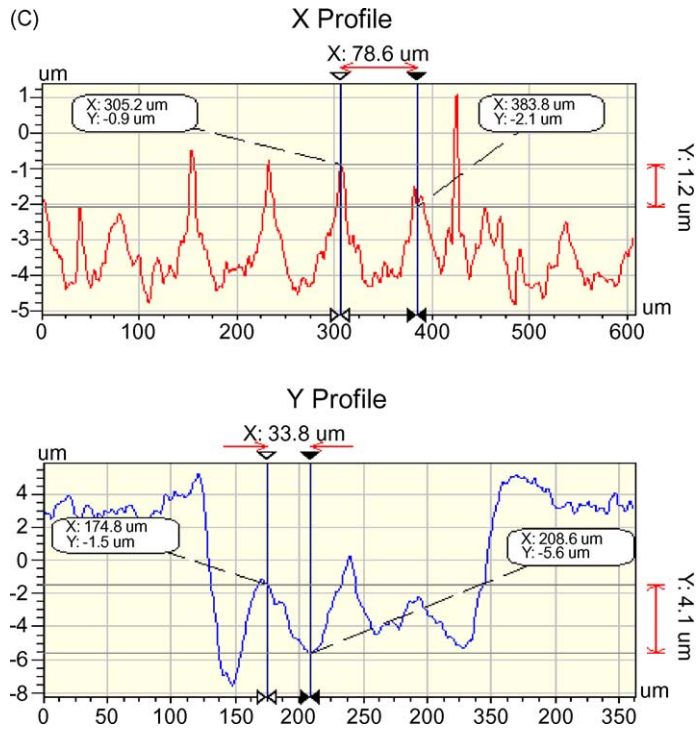


Fig. 5. (Continued).

heat affected zone and with a potential reduction in residual surface roughness for a given depth.

That this is indeed the case is shown by Figs. 9 and 10 where we have reduced laser fluence to  $F \sim 1.4 \text{ J cm}^{-2}$  and average scanned power density

$\sim 3.3 \text{ W cm}^{-2}$ . Fig. 9 shows the measured ablation depth as a function of number of overscans which, as expected, is linear ( $0.63 \mu\text{m}$  per overscan). Fig. 10 shows that residual roughness grows to approximately  $1.15 \pm 0.1 \mu\text{m}$  at a channel depth of  $\sim 50 \mu\text{m}$  while

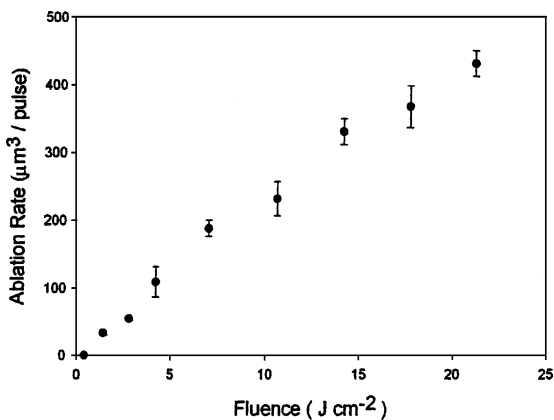


Fig. 6. Measured volume ablation rate per pulse vs. fluence (at  $10 \text{ mm s}^{-1}$  scan speed).

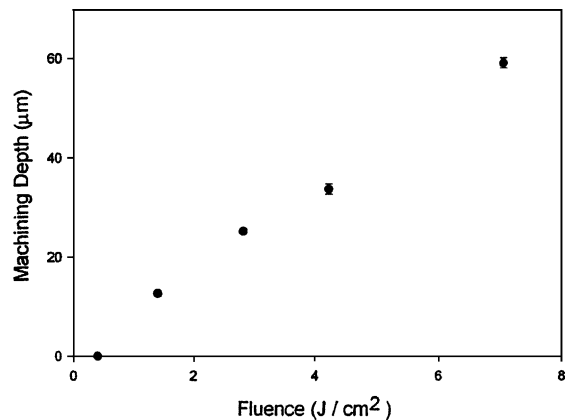


Fig. 7. Channel depth vs. fluence for 20 overscans at  $10 \text{ mm s}^{-1}$  scan speed. (average power  $0\text{--}17 \text{ W cm}^{-2}$  with  $10 \mu\text{m}$  raster).

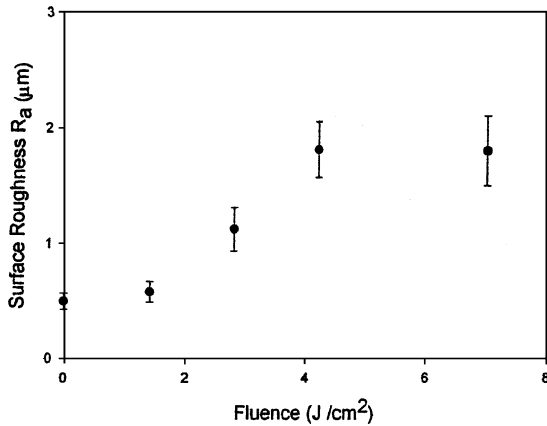


Fig. 8. Channel surface roughness  $R_a$  vs. fluence for 20 overscans at 10 mm s<sup>-1</sup> scan speed (average power 0–17 W cm<sup>-2</sup> with 10 µm raster).

micro-machining to the same depth at  $F \sim 7 \text{ J cm}^{-2}$  ( $\sim 17 \text{ W cm}^{-2}$ ) yields a surface roughness of  $1.8 \pm 0.4 \text{ µm}$  (Figs. 7 and 8). Both roughness  $R_a$  and  $\sigma(R_a)$  grow with increasing fluence. There is a clear advantage in micro-machining aluminium near ablation threshold and low average power density. At fluence  $F \sim 1.4 \text{ J cm}^{-2}$ , the effect of ablating as little as  $\sim 50 \text{ nm}$  per pulse translates the initial surface relief to  $>30 \text{ µm}$  depth in the material, demonstrated with the WYKO surface profiler and SEM images (e.g., Fig. 2(h) and Fig. 4(a)). Eventually, the small amount of material re-deposition coupled with the slightly higher ablation rate at the centre of

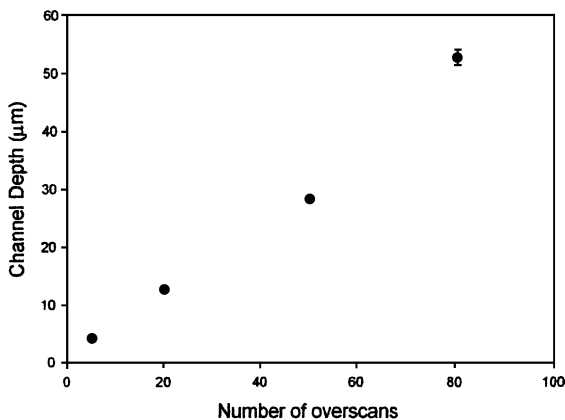


Fig. 9. Channel depth vs. number of overscans micro-machined at  $\sim 3.3 \text{ W cm}^{-2}$  average power ( $1.4 \text{ J cm}^{-2}/10 \text{ mm s}^{-1}$ ).

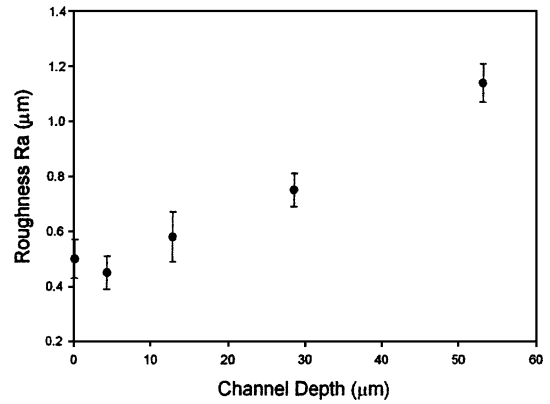


Fig. 10. Channel surface roughness  $R_a$  vs. depth micro-machined at  $\sim 3.3 \text{ W cm}^{-2}$  average power ( $1.4 \text{ J cm}^{-2}/10 \text{ mm s}^{-1}$ ).

grooves wipes out the history of the initial surface relief.

The nature of the debris generated at low fluence and average power was investigated briefly by collecting this nearby on a lacey carbon-coated TEM grid. Spherical pure aluminium particles ranging in size from  $\sim 10$  to  $\sim 200 \text{ nm}$  diameter were observed, confirmed by TEM and EDX while electron diffraction showed these were single crystal in nature. The mechanisms of formation of nanoparticles from hot plasma in the presence of helium will be studied further.

#### 4. Conclusions

Aluminium presents a particular challenge to laser surface micro-structuring, even with femtosecond optical pulses. This is a consequence of its relatively low melting point and high thermal conductivity combined with its tendency to rapidly oxidise. The use of flowing helium is of major benefit when micro-structuring aluminium with NIR femtosecond laser radiation, minimising plasma breakdown and surface oxidation and helps to remove fine debris.

Residual thermal effects are significant at high average power densities  $>85 \text{ W cm}^{-2}$  resulting in thermal degradation and hence a very poor level of material processing. On the contrary, much superior micro-structuring was achieved at low average power density  $\langle I \rangle \sim 3.3 \text{ W cm}^{-2}$  combined with low single pulse fluence ( $1.4 \text{ J cm}^{-2}$ ) producing residual surface

roughness of  $\sim 1 \mu\text{m}$  rms at  $\sim 50 \mu\text{m}$  depth. Volume ablation rate of aluminium at fluence  $F \sim 1.4 \text{ J cm}^{-2}$  is  $\sim 33 \mu\text{m}^3$  per pulse indicating an ablation depth  $d \sim 50 \text{ nm}$  per pulse. While re-deposition is also minimised at ambient pressure under these conditions, nevertheless, this fine condensed material arriving back at the surface is responsible for the developing periodic surface relief at the base of micro-machined channels, independent of the initial surface roughness.

At fluence  $F \sim 7 \text{ J cm}^{-2}$  and average power density  $\sim 33 \text{ W cm}^{-2}$ , the ablated surface developed round pits up to  $15 \mu\text{m}$  wide and  $\sim 10 \mu\text{m}$  deep at a machined depth of  $\sim 35 \mu\text{m}$  and sensitive to both incident polarisation state and initial surface roughness. This effect is much less prevalent as pulse fluence is reduced.

Single pulse ablation demonstrates surface melting above  $F \sim 4 \text{ J cm}^{-2}$  and hence that low single pulse fluence combined with low average power density  $< 5 \text{ W cm}^{-2}$  points to an optimum regime for femto-second laser processing, minimising melt and residual thermal effects. Clearly, at fluences well above the ablation threshold, surface melting occurs, leading to a larger HAZ and negating the advantages possible with ultra-fast micro-machining [24]. Even at low fluence, a thin residual melt layer remains, and may cool rapidly to produce an amorphous layer [25].

The nature of debris generated during ultra-fast laser processing of aluminium under helium is highly dependent on both laser pulse fluence and average scanned power density and becomes much finer as these parameters are reduced. Near ablation threshold and  $\langle I \rangle \sim 3.3 \text{ W cm}^{-2}$ , we have observed spherical nanometer size aluminium single crystal particles carried with the helium stream.

Ablation threshold for aluminium  $F_{\text{th}} \sim 0.4 \text{ J cm}^{-2}$  for 180 fs pulses at 775 nm and this value agrees approximately with those obtained for measurements of single pulse exposure at 125 and 33 fs of between 0.3 and  $0.5 \text{ J cm}^{-2}$  [14,15].

## Acknowledgements

We would like to thank Mr. Lawrence Bailey and Mr. Richard Arnold of the Department of Engineering,

University of Liverpool for their technical assistance during this work.

## References

- [1] C. Momma, B.N. Chichkov, S. Nolte, F. von Alvensleben, A. Tunnermann, H. Welling, B. Wellegenhausen, *Opt. Commun.* 128 (1996) 101–109.
- [2] W. Kautek, J. Kruger, *Mater. Sci. Forum* 173/174 (1995) 17–22.
- [3] W. Kautek, J. Kruger, *SPIE* 2207 (1994) 600–611.
- [4] J. Kruger, W. Kautek, *Appl. Surf. Sci.* 106 (1996) 383–389.
- [5] S. Kuper, M. Stuke, *Appl. Phys. B* 44 (1987) 199–204.
- [6] D. Stern, R.W. Schoenlein, C.A. Puliafito, E.D. Dobi, R. Birngruber, J.G. Fujimoto, *Arch. Ophthalmol.* 107 (1989) 587–592.
- [7] J. Ihlemann, B. Wolff, P. Simon, *Appl. Phys. A* 54 (1992) 363–368.
- [8] N. Rizvi, *Riken Rev.* 50 (2003) 107–112.
- [9] E.G. Gamaly, A.V. Rode, V.T. Tikhonchuk, B. Luther-Davies, *Appl. Surf. Sci.* 197/198 (2002) 699–704.
- [10] F. Muller, K. Mann, P. Simon, *SPIE* 1858 (1993) 464–475.
- [11] A. Cairns, *Micro Laser Cutting Project Report*, EPSRC Ref. GR/M11738, MEIM, Department of Engineering, University of Liverpool, February 2000.
- [12] X. Zhu, A. Yu. Naumov, D.M. Villeneuve, P.B. Corkum, *Appl. Phys. A* 69 (Suppl.) (1999) S367–S371 (COLA'99).
- [13] M. Lapczyna, K.P. Chen, P.R. Herman, H.W. Tan, R.S. Marjoribanks, *Appl. Phys. A* 69 (Suppl.) (1999) S883–S886 (COLA'99).
- [14] J. Kruger, P. Meja, M. Autric, W. Kautek, *Appl. Surf. Sci.* 186 (2002) 374–380.
- [15] S. Martin, J. Kruger, A. Hertwig, A. Fiedler, W. Kautek, *Appl. Surf. Sci.* 208/209 (2003) 333–339.
- [16] W.M. Steen, *Laser Material Processing*, Springer, Berlin, 1998.
- [17] J. Sun, J.P. Longtin, *J. Appl. Phys.* 89 (12) (2001) 8219–8224.
- [18] D. Strickland, G. Mourou, *Opt. Commun.* 56 (1985) 219–221.
- [19] S. Ameer-Beg, W. Perrie, S. Rathbone, J. Wright, W. Weaver, H. Champoux, *Appl. Surf. Sci.* 127–129 (1998) 875–880.
- [20] K. Animesh, V.N. Kulkarni, D.K. Sood, J.S. Uppal, *J. Appl. Phys.* 52 (7) (1981) 4882–4884.
- [21] A. Boroweic, H.K. Haugen, *Appl. Phys. Lett.* 82 (25) (2003) 4462–4464.
- [22] E.D. Palik (Ed.), *Handbook of Optical Constants of Solids*, Academic Press, New York, 1985.
- [23] B. Rethfeld, A. Kaiser, M. Vicanek, G. Simon, *Appl. Phys. A* 69 (Suppl.) (1999) S109–S112 (COLA'99).
- [24] A. Luft, U. Franz, A. Emsemann, J. Kasper, *Appl. Phys. A* 63 (1996) 93–101.
- [25] Y. Hirayama, M. Obara, *Appl. Surf. Sci.* 197/198 (2002) 741–745.